

Dynamically Interfacial pH-Buffering Effect Enabled by *N*-Methylimidazole Molecules as Spontaneous Proton Pumps toward Highly Reversible Zinc-Metal Anodes

Minghao Zhang, Haiming Hua, Pengpeng Dai, Zheng He, Lianhuan Han, Peiwen Tang, Jin Yang, Pengxiang Lin, Yufei Zhang, Dongping Zhan, Jianken Chen, Yu Qiao, Cheng Chao Li,* Jinbao Zhao,* and Yang Yang*

Aqueous zinc-metal batteries have attracted extensive attention due to their outstanding merits of high safety and low cost. However, the intrinsic thermodynamic instability of zinc in aqueous electrolyte inevitably results in hydrogen evolution, and the consequent generation of OH^- at the interface will dramatically exacerbate the formation of dead zinc and dendrites. Herein, a dynamically interfacial pH-buffering strategy implemented by *N*-methylimidazole (NMI) additive is proposed to remove the detrimental OH^- at zinc/electrolyte interface in real-time, thus eliminating the accumulation of by-products fundamentally. Electrochemical quartz crystal microbalance and molecular dynamics simulation results reveal the existence of an interfacial absorption layer assembled by NMI and protonated NMI (NMIH^+), which acts as an ion pump for replenishing the interface with protons constantly. Moreover, an in situ interfacial pH detection method with micro-sized spatial resolution based on the ultra-microelectrode technology is developed to probe the pH evolution in diffusion layer, confirming the stabilized interfacial chemical environment in NMI-containing electrolyte. Accordingly, with the existence of NMI, an excellent cumulative plating capacity of 4.2 Ah cm^{-2} and ultrahigh Coulombic efficiency of 99.74% are realized for zinc electrodes. Meanwhile, the NMI/ NMIH^+ buffer additive can accelerate the dissolution/deposition process of $\text{MnO}_2/\text{Mn}^{2+}$ on the cathode, leading to enhanced cycling capacity.

1. Introduction


Lithium-ion batteries (LIBs) have experienced expeditious progress in the past two decades, and successfully dominated power sources in portable electronics and electric vehicles.^[1] However, the unsatisfactory safety performance of LIBs owing to the utilization of toxic and flammable carbonated-based electrolytes limits their further applications in emerging grid-scale energy storage devices, which has also motivated extensive efforts seeking high-safety, cost-effective, and environmentally friendly battery technologies.^[2] Benefitting from the advantages of zinc metal such as low redox potential (-0.76 V , vs standard hydrogen electrode (SHE)), high theoretical specific capacity (820 mAh g^{-1}), low cost, and good compatibility with aqueous electrolyte, aqueous zinc-metal batteries (AZMBs) with metallic Zn as anode are considered to be one of the most promising candidates.^[3] However, the commercialization of high-performance AZMBs are still hindered by dendrite growth, hydrogen evolution, and formation of by-products on the surface of Zn metal.^[4] Particularly, the continuous accumulation of

by-products accompanied by hydrogen evolution side reaction will lead to tremendous insulating sites on the surface of Zn anode, which will dramatically exacerbate the rampant growth of dendrites or surface passivation, increasing the battery polarization and then aggravate the hydrogen evolution reaction (HER) (Figure 1a).^[5]

In order to alleviate the deterioration of Zn anode, researchers have addressed tremendous efforts, such as building conductive hosts,^[6] surface modification,^[7] and regulating the electrolyte.^[8] Among these strategies mentioned above, design of electrolytes by additives engineering has attracted extensive attention due to the outstanding merits of simpleness, efficiency, and cost-effectiveness.^[9] Various functional additives like 1,2-dimethoxyethane,^[10] glucose,^[11] and diethyl ether^[12] have been reported to be capable of suppressing the dendrite growth and parasitic reactions through forming

M. Zhang, H. Hua, P. Dai, Z. He, L. Han, P. Tang, J. Yang, P. Lin, D. Zhan, J. Chen, Y. Qiao, J. Zhao, Y. Yang
State Key Lab of Physical Chemistry of Solid Surfaces
State-Province Joint Engineering Laboratory of Power Source Technology for New Energy Vehicle
College of Chemistry and Chemical Engineering
Xiamen University
Xiamen 361005, P. R. China
E-mail: jbzhaoy@xmu.edu.cn; yangyang419@xmu.edu.cn

Y. Zhang, C. C. Li
School of Chemical Engineering and Light Industry
Guangdong University of Technology
Guangzhou 510006, P. R. China
E-mail: licc@gdut.edu.cn

 The ORCID identification number(s) for the author(s) of this article can be found under <https://doi.org/10.1002/adma.202208630>.

DOI: 10.1002/adma.202208630

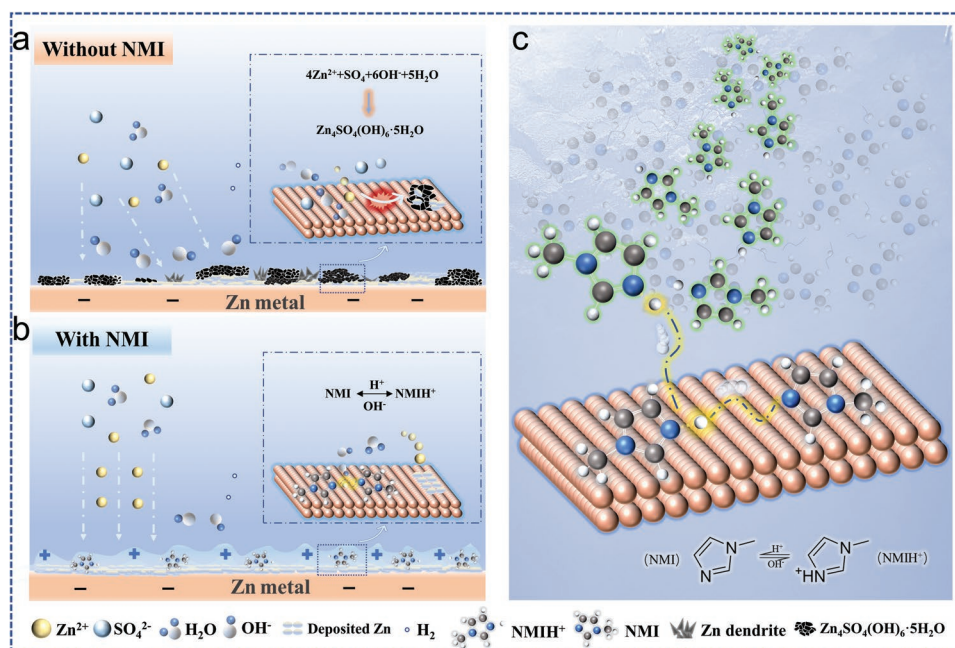


Figure 1. a–c) Schematic illustrations of the deterioration of Zn anode in pure ZnSO₄ electrolyte (a), NMI additive improving the reversibility of Zn anode (b), and the proton-transfer process between NMI additive molecules (c).

H-bonding, modulating solvation structure, and building electrostatic shields.^[9,13] From a thermodynamical view, however, the standard electrode potential of hydrogen evolution reaction is 0 V while the zinc reduction is much lower (−0.76 V vs SHE), which means that the occurrence of hydrogen evolution during Zn deposition process cannot be completely avoided.^[10,14] Meanwhile, the inevitable hydrogen evolution especially under high-rate cycling conditions will trigger the local alkaline environment at the electrode–electrolyte interface, resulting in the formation of irreversible by-products ($\text{Zn}_4\text{SO}_4(\text{OH})_6 \cdot 5\text{H}_2\text{O}$, ZSH).^[7a,9] Therefore, some inspiring works have been conducted to reduce the pH change of bulk electrolytes to extend the lifespan of Zn-metal anodes.^[15] Nonetheless, the research of stabilizing pH at the localized Zn interface region is still at its fancy stage, and more in-depth mechanism and methodology validation are necessary.

In this work, a dynamically interfacial pH-buffering strategy enabled by an *N*-methylimidazole (NMI) additive is proposed to eliminate the formation of ZSH on the surface of Zn-metal anodes. As shown in Figure 1b, the absorption buffer layer assembled by NMI and protonated *N*-methylimidazole (NMIH⁺), can not only release protons to clear up ZSH intensively and immediately, but also restrict the 2D migration of Zn²⁺ to inhibit the dendrite growth, thus markedly improving the reversibility of Zn anode. Moreover, benefitting from the direct and rapid proton-transport kinetics between NMI and NMIH⁺ molecules, an uninterrupted and fast proton-transport network together with water molecules is established in electrolytes. Therefore, NMI molecules can work as spontaneous ionic pumps to transport protons continuously from bulk phase to the interface region (Figure 1c), thereby stabilizing the interfacial pH dynamically. Furthermore, the pH evolution of interface region during Zn deposition process is also detected in situ by scanning electrochemical microscopy coupled with

pH ultra-microelectrode, revealing the dramatic pH increase at interface region in conventional 2.0 M ZnSO₄ electrolyte, and confirming the effective diminishment of interfacial pH change with the existence of NMI. In addition to the highly reversible Zn deposition behavior, the NMI/NMIH⁺ buffer additive is also unexpectedly found to accelerate the dissolution/deposition kinetics of MnO₂/Mn²⁺ through releasing or capturing protons on the cathode during cycling, leading to the enhanced reversible capacity and cycling stability. The proposed interfacial pH-buffering strategy should provide a significant guideline for the further development of practical AZMBs.

2. Results and Discussion

Since the increased pH of electrolyte will lead to the formation of ZSH while the decreased pH will exacerbate the HER, maintaining the stable pH value of electrolyte and reaction interface has a crucial impact on the performance of Zn anode.^[16] As shown in Figure 2a, the buffer platform of NMI in 2.0 M ZnSO₄ is between 3.6 and 5.4, and ZSH dissolves when 20% NMI is neutralized. The realization of buffering effect depends on the reversible binding and releasing of H⁺ from 3-nitrogen atom at NMI molecule. With the pH of the solution decreasing from 5.2 to 3.0, the intensities of Raman peaks located at 1235 cm^{−1}, 1350 cm^{−1}, and 1422 cm^{−1} decrease while intensities of peaks located at 1288 cm^{−1} and 1457 cm^{−1} increase^[17] (Figure S1a, Supporting Information), demonstrating the transition from NMI to NMIH⁺. In addition, the decrease of absorbance at 290 nm in UV spectrum (Figure S1b, Supporting Information) also suggests the transition from NMI to NMIH⁺, revealing the concentration ratio of NMI to NMIH⁺ is correlated with the pH of solution. In the subsequent works, the pH of NMI + 2.0 M ZnSO₄ is adjusted to 4.0 to be consistent with the pH

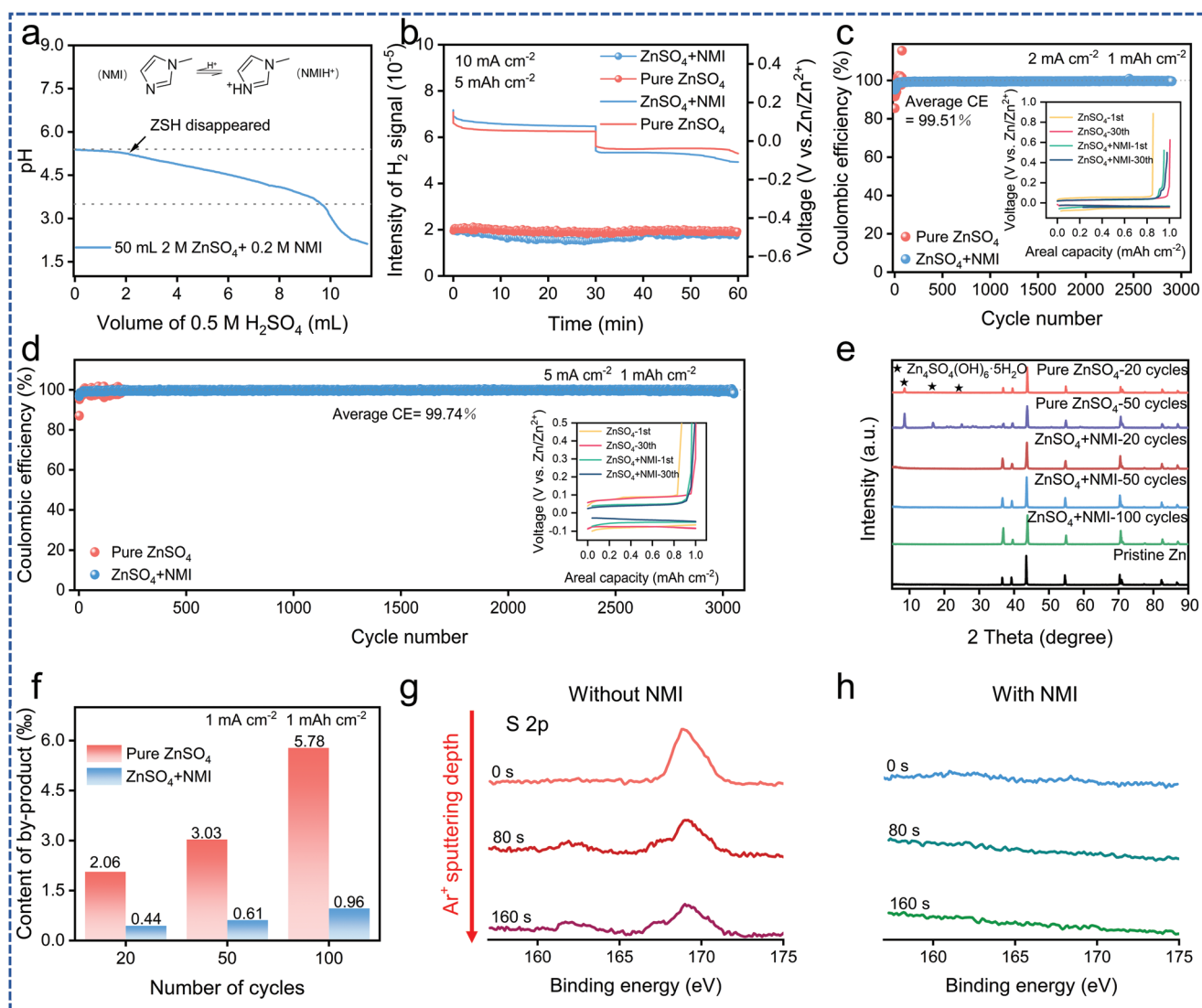


Figure 2. a) Acid–base titration curve of 2.0 M ZnSO_4 with the addition of 0.2 M NMI. b) In situ monitoring of hydrogen evolution and its corresponding time–voltage curve in Zn//Zn symmetric cells with different electrolytes. c, d) CE of $-\text{Zn}/\text{Cu}$ half cells (the insets show the galvanostatic voltage profiles) at 2.0 mA cm^{-2} (c) and 5.0 mA cm^{-2} (d) with the Zn plating capacity of 1.0 mAh cm^{-2} . e) XRD patterns of pristine Zn foil and Zn foils cycled in different electrolytes at 1.0 mA cm^{-2} for 1.0 mAh cm^{-2} . f) Contents of ZSH in Zn foils tested by ion chromatography. g, h) S 2p XPS spectra depth profile of the Zn foil cycled in ZS (g) and NZ (h).

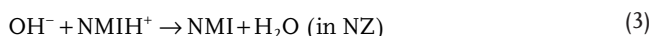
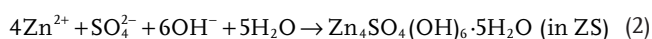
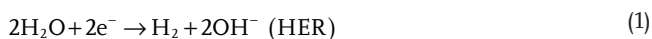
of pure 2.0 M ZnSO_4 . Therefore, for the 50 mL 0.2 M NMI + 2.0 M ZnSO_4 solution, the valid section for pH buffering corresponding to 2–9 mL 0.5 M H_2SO_4 from the titration curve, indicating a utilization rate of more than 70% while using NMI as a buffer additive. In situ differential electrochemistry mass spectroscopy (DEMS, Figure S2, Supporting Information) with a homemade electrochemistry cell is performed to monitor the formation of hydrogen during the electrochemical deposition of Zn. As shown in Figure 2b, with the addition of 0.2 M NMI, the hydrogen evolution rate is slightly reduced. Besides, the addition of NMI slightly increases the hydrogen evolution overpotential of the Zn electrode from the hydrogen evolution test (Figure S3, Supporting Information), suggesting the addition of NMI will not exacerbate the hydrogen evolution reaction. Therefore, the improved performance of Zn anode can be attributed

to the dynamically interfacial pH-buffering effect, revealing the significance of inhibiting the accumulation of ZSH.

Subsequently, 2.0 M ZnSO_4 with different concentrations of NMI (0, 0.05, 0.1, 0.2, and 0.5 M) are employed as the electrolytes of Zn//Zn symmetric cells (Figure S4, Supporting Information), and Zn//Cu half cells (Figure S5, Supporting Information) to determine the optimum additive concentration. Clearly, there are still some dendrites accumulated on the surface of cycled Zn foil with the low addition of NMI (Figure S6, Supporting Information) and the Zn//Zn symmetric cells fail due to the short circuit when employing electrolytes with a low concentration of NMIH^+ (0, 0.05 M, 0.1 M). However, the coulombic efficiency (CE) of Zn//Cu half cells will decrease as the concentration of NMIH^+ increases owing to the increased electrode polarization. It can be speculated that

the concentration of NMI in bulk phase will affect the cyclic performance by changing the proton reserve in bulk phase and amount of NMIH⁺ adsorbed on the rapidly changing surface. Based on the above test results, 2.0 m ZnSO₄ with 0.2 m NMI (named as NZ) was chosen as the target electrolyte component.

Zn//–Cu half cells are assembled to evaluate the reversibility of Zn anode. With a plating/stripping capacity of 1.0 mAh cm⁻², half cells employing NZ electrolyte deliver an ultrahigh average CE of 99.51% during 3000 cycles at a current density of 2.0 mA cm⁻² (Figure 2c) and 99.74% at 5.0 mA cm⁻² (Figure 2d), while the half cells with mild acidic pure ZnSO₄ electrolyte (named as ZS) failed rapidly and shown fluctuating CE in less than 100 cycles due to the accumulation of dead zinc and ZSH. Besides, when the thickness of Zn foils is reduced to 10 μm and 20 μm, Zn//–Cu half cells with NZ electrolyte can also exhibit higher CE in more stable cycles (Figure S7, Supporting Information). Therefore, X-ray diffraction (XRD) is employed to identify the existence of ZSH, the root of dead zinc accumulation, and poor Zn plating/stripping reversibility. As shown in Figure 2e, compared with pure Zn metal, several obvious peaks which are indexed to ZSH appear at ≈ 8.1°, 16.2°, and 24.4° 2θ (JCPDS: 78-0246) after 20 and 50 cycles of Zn foil in ZS. In contrast, there are no obvious peaks in XRD pattern of the Zn foil in NZ over 100 cycles. Moreover, the content of ZSH is determined by quantifying sulfate ions in Zn foils with ion chromatography. As revealed in Figure 2f, after 20, 50, and 100 cycles, the contents of ZSH in Zn foils cycling with pure ZS are 2.06‰, 3.03‰, and 5.78‰, respectively. By contrast, the contents of ZSH are significantly reduced (0.44‰, 0.61‰, and 0.96‰, respectively) with the existence of NMI, indicating the interfacial pH-buffering strategy can improve the reversibility of zinc anode by eliminating the formation of ZSH. In addition, with the increase of NMI addition, the content of ZSH on Zn electrode decreases significantly (Figure S8, Supporting Information), revealing that the buffer effect is related to the concentration of NMI in bulk phase due to the proton reserve and absorption in the changing interface. Furthermore, the chemical composition of deposited Zn is evaluated by XPS (X-ray photoelectron spectroscopy). As shown in Figure 2g, the obvious peak at 168.2 eV in S 2p spectrum implies the existence of ZSH on Zn electrodes cycled in ZS. Moreover, S element can still be detected after etching by Ar⁺ sputtering for 80 s or 160 s, representing the intergrowth of loosely deposited Zn and ZSH. In sharp contrast, no obvious peak appears in S 2p spectrum of Zn electrodes cycled in NZ (Figure 2h), confirming that NMI additive can clear the newly generated OH⁻ continuously at interface during charge–discharge process. According to above works, the evolution of OH⁻ in ZS and NZ can be described as follows:



Considering that both the Zn deposition and the formation of ZSH take place at the electrode–electrolyte interface region, the stable dynamic adsorption layer at interface is a prerequisite

for the realization of local buffer strategy and limiting 2D diffusion of zinc ions. Therefore, (Electrochemical) quartz crystal microbalance ((E) QCM), which can sensitively reflect the mass change of electrode by the change in frequency of quartz crystal,^[18] is carried out to assess the adsorption behavior of additive on electrode interface. As shown in Figure 3a, inert Au quartz electrodes are used in EQCM to detect the mass changes at different potentials and Au@Zn electrodes (Figure S9, Supporting Information) with Zn deposited by atomic layer deposition are used in QCM to evaluate the specific adsorption of additive. In the QCM tests (Figure 3b), as the baseline has gone flat, 0.2 m Na₂SO₄ is added to the electrolyte. It is observed that the vibration frequency changes sharply after an external liquid shock and then remains constant quickly, suggesting that the system can quickly recover from a disturbance. When 0.2 m (NMIH)₂SO₄ under the same conditions is added, after a drastic change caused by shock, the vibration frequency continuously increases by 32 Hz. It means that the apparent mass of electrode is decreased by 44.8 ng, revealing the continuous migration of additive from the bulk phase to the interface.^[19] Organic molecules like NMIH⁺ adsorbed on the interface will occupy a very large surface space on Zn anode, and replace several layers of much smaller but well-oriented water molecules, thus decreasing the density of the interfacial electrolyte,^[20] leading to the reduced apparent mass of Zn electrode. Moreover, the vibration frequency of Zn electrode remains constant even after more (NMIH)₂SO₄ is added to the electrolyte, confirming the saturated state of NMIH⁺ adsorption layer. Besides, influences like the density of electrolytes could be excluded due to the stable frequency in this step. In addition, a similar trend is obtained from QCM test under the same condition in 0.2 m ZnSO₄ (Figure 3c) and 2.0 m ZnSO₄ (Figure S10, Supporting Information), elucidating that additive can indeed affect the density of interfacial electrolyte on the Zn surface through specific adsorption of NMI and NMIH⁺ which is undisturbed by cation species either Na⁺ or Zn²⁺. Differential capacitance (DC) and electrochemical impedance spectroscopy (EIS) tests are also conducted to further confirm the adsorption species. With the increase of NMIH⁺ content in interface reflected by the decrease of pH, the right shift of capacitance peak in DC curve (Figure S11, Supporting Information)^[21] and the increase of charge-transfer resistance (*R*_{ct}) in EIS (Figure S12, Supporting Information) is observed, directly indicating the existence of NMIH⁺ in the electric double layer. Since both NMIH⁺ and Zn²⁺ are cations, the *R*_{ct} will also increase due to the repulsion between like-charged ions, which will make it more difficult for Zn²⁺ to cross the absorption layer, thus proving that NMIH⁺ is indeed involved in the adsorption at the interface.^[22] Tafel curves in Figure 3d exhibit significantly increased corrosion potential and decreased corrosion current, which are in good consistent with the absorption of additive. Besides, the contact angle test (Figure S13, Supporting Information) shows that the addition of NMI in electrolyte can notably reduce the contact angle (from 53.99° to 38.35°) with the polished zinc foil due to the increased interfacial residual charge which is derived from the absorption of NMIH⁺.

Moreover, EQCM test of Au electrode is applied to monitor the in situ mass change of electrode interface at different potentials in practical batteries, and 0.2 m Na₂SO₄ aqueous

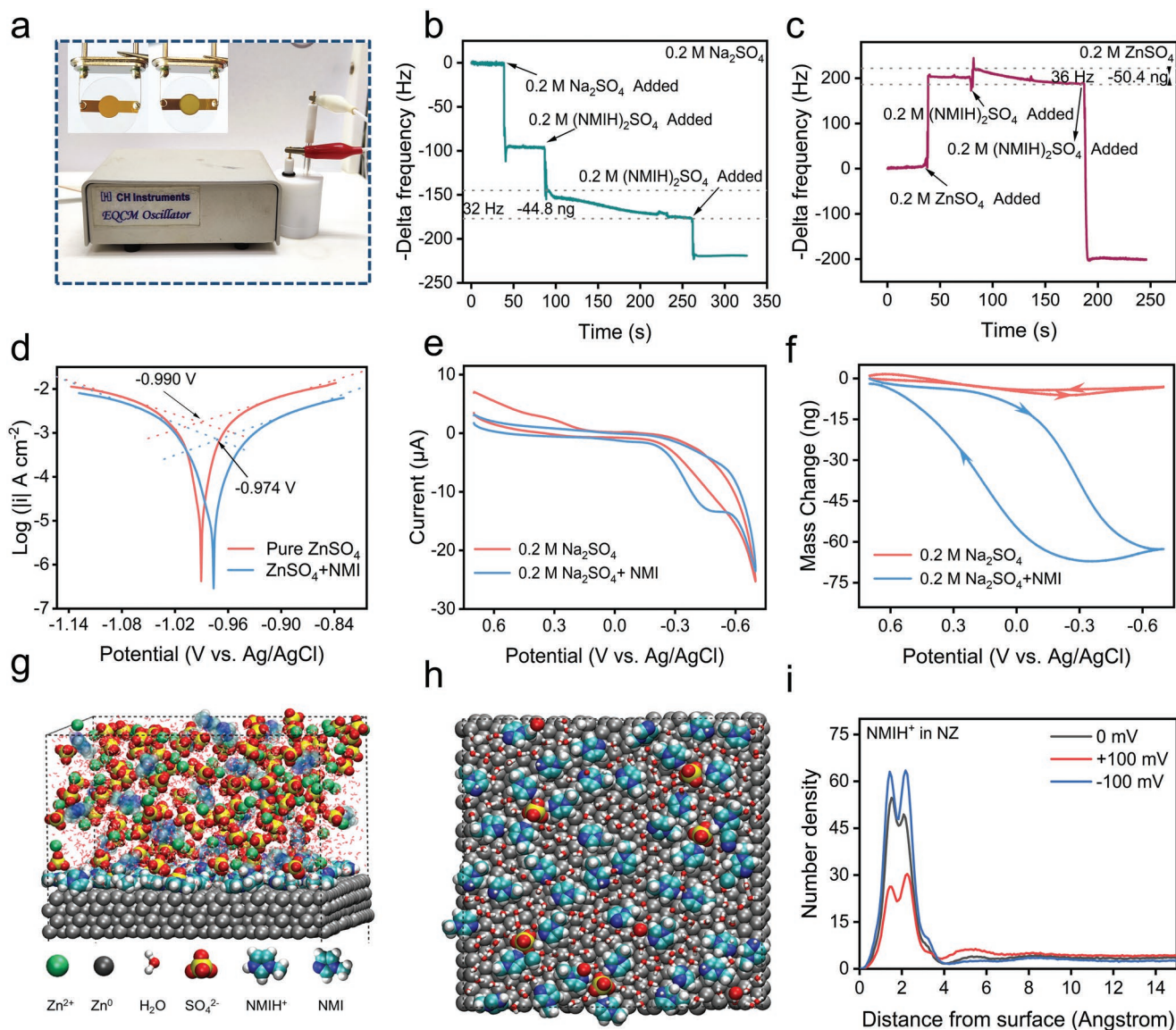


Figure 3. a) Digital image of in situ QCM/EQCM equipment (left of insets is the Au-sputtered circular quartz substrate and the right is Zn QCM electrode). b,c) QCM tests in 0.2 M Na_2SO_4 solution (b) and 0.2 M ZnSO_4 solution (c). d) Tafel plots of Zn electrode tested in NZ and ZS. e,f) EQCM test using Au QCM electrode as substrate in 0.2 M Na_2SO_4 with/without NMI additive. e) Cyclic voltammograms (CV) curves and f) corresponding mass change. g–i) Classical molecular dynamics simulation of species distribution of NZ in Zn electrode–electrolyte interface region. g) Side view and h) top view of species distribution. i) Concentration distribution of NMI in the interfacial region at different potentials.

solution was adopted as the supporting electrolyte to eliminate the disturbance of Zn deposition/dissolution in ZnSO_4 electrolyte. As depicted in Figure 3e, CV curves of two electrolytes with and without NMI added are basically similar, which are both contributed to the adsorption–desorption of hydrogen atoms.^[23] However, there is a distinct difference in mass change between these two electrolytes (Figure 3f). In a pure 0.2 M Na_2SO_4 electrolyte, the tiny mass change at different potentials is contributed to the competitive adsorption of H atoms with H_2O molecules on the interface and trace dissolution of surface Au.^[22] By comparison, there is a significant mass change for Au electrode in 0.2 M Na_2SO_4 + NMI electrolyte when the potential changes, which is attributed to the adsorption of NMIH^+ on the interface at low potential and the desorption of NMIH^+

at high potential due to the electrostatic interaction. The EQCM results illustrate that the electric field can drive NMIH^+ close to the interface and increase the interfacial concentration of additive, which will be beneficial to the migration of protons from NMIH^+ in bulk phase to NMI at interface through the rapidly hopping process.^[24]

To obtain deeper insight into the electrochemical interface, classical molecular dynamics (MD) simulation is carried out to investigate the distribution and adsorption behavior of species at the interface. Apparently, abundant H_2O molecules and SO_4^{2-} ions are adsorbed on the surface of Zn metal at zero charge potential (Figure S14, Supporting Information). The interfacial H_2O molecules are more easily to be split up to form H_2 and OH^- , which will combine with Zn^{2+} and SO_4^{2-} ions in the

interface region, leading to the accumulation of by-products. Apparently, numerous NMI and NMIH⁺ ions are adsorbed at the interface after the addition of NMI additive (Figure 3g-h), which is consistent with the above experimental results. Simultaneously, a considerable amount of sulfate ions and H₂O molecules are excluded from the interface (Figure S15, Supporting Information), indicating a good agreement with the increase of hydrogen evolution overpotential. Moreover, the adsorption behavior of additives at different potentials is simulated by MD. As shown in Figure 3i, the adsorption amount of NMIH⁺ increases significantly with the decrease of electrode potential, indicating that there will be more NMIH⁺ ions absorbed on the interface due to the electrostatic effect during Zn deposition process.

The interfacial buffering strategy will inevitably be accompanied by the loss of protons in NMIH⁺. Therefore, it is necessary for protons to be continuously transported to the interface layer thus maintaining the dynamic buffering effect. In order to reveal the concrete behavior of protons and NMI additive in the interfacial pH-buffering strategy, quantum chemistry calculation is performed to compare the activation Gibbs free energy (ΔG^\ddagger) of different proton-transport processes. As shown in Figure 4a, ΔG^\ddagger of proton-transport process through “NMIH–NMI” transition state is close to 0 kJ mol⁻¹, which is much smaller than ΔG^\ddagger through “NMIH–H₂O–NMI” or “NMIH–H₂O–H₂O–NMI”, indicating the rapid proton-transport kinetics between NMI molecules.^[24] Furthermore, MD calculation shows the diffusion coefficient of NMIH⁺ at interface is only 0.031×10^{-5} cm² s⁻¹ (Figure 4b), demonstrating the difficulty of subsequent adsorption–desorption process of NMIH⁺ or NMI at the interface. In the practical process of zinc deposition, the rate of hydrogen evolution is less than the rate of proton transfer in bulk phase. Therefore, the key to the dynamic buffering effect is the rapid proton conductive process at the interface. Although the diffusion coefficient of H₃O⁺ (9.34×10^{-5} cm² s⁻¹) is higher than that of NMIH⁺ (0.53×10^{-5} cm² s⁻¹), due to the much higher concentration of NMIH⁺ (0.18 M, 90% protonation of NMI) than H₃O⁺ (1.0×10^{-4} M, pH = 4) and the absorption enrichment effect, interfacial NMI prefers to acquire protons directly from the neighboring NMIH⁺ to renew the buffer adsorption layer once the proton of interfacial NMIH⁺ is consumed, in which the protons are described as “hopping” from NMIH⁺ to NMI directly. The calculation results in Figure 4a also reveal that there will be a higher ΔG^\ddagger when protons diffuse along longer water molecules chain. In the bulk phase, considering the mechanism of Grotthuss diffusion^[25] in water and the high concentration of NMIH⁺, it can be speculated the proton carrier NMIH⁺ can act as a node in aqueous hydrogen-bonded system, forming a fast proton transferring network together with water molecules, (Figure S16, Supporting Information) thus shortening the path of proton transport. Consequently, the NMI additive builds up a proton warehouse and transport network in electrolyte, in which the NMIH⁺ ions act as spontaneous proton pumps toward maintaining the dynamically interfacial pH-buffering effect.

In order to evaluate the pH evolution as well as the interfacial pH-buffering effect, scanning electrochemical microscopy (SECM) equipped with ternary pH ultra-microelectrode (UME) is developed for the in situ pH determination in diffusion

layer in our home-made electrochemical cell (Figure 4c; Figure S17, Supporting Information), which has barely been reported in previous studies. The pH ultra-microelectrode consists of 50 μ m diameter W/WO₃^[26] and Ag/AgCl electrodes and a 20 μ m diameter Pt electrode, which serves as a pH microsensor, reference electrode, and distance positioner, respectively, making the ultra-microelectrode can simultaneously realize distance control and pH detection.^[27] Besides, the integrated strategy of Ag/AgCl reference electrode and W/WO₃ pH-detecting electrode can effectively reduce the interference of solution resistance and electric field.^[28] As a conductive metal substrate, Zn foil has a positive feedback effect on the oxidation of ferrocene methanol (FcMeOH) under diffusion-limited conditions.^[29] As shown in Figure 4d, the closer the Pt UME approaches the substrate, the higher the oxidation current is, which is attributed to the catalysis of substrate on the FcMeOH transformation from oxidation state to reduction state.^[30] The distance between Pt electrode and Zn substrate is ≈ 0.8 times the electrode radius (8 μ m) when the current reaches 1.5 times the steady-state current in bulk phase.^[31] And the distance is enough for the deposition of Zn. As presented in Figure 4e, the vertical distance between Pt electrode and the W/WO₃ electrode is ≈ 20 μ m, thus the distance between pH UME and Zn substrate can control at 30 μ m, which is less than the thickness of the diffusion layer.^[32]

Figure 4g shows the pH evolution in diffusion layer or bulk phase in NZ and ZS electrolytes during the electrodeposition process. Obviously, the pH of diffusion layer in ZS electrolyte increased rapidly to 5.1 in 800 s and remained constant during electrodeposition, indicating the accumulation of OH⁻ at interface region and subsequent consumption due to the continued formation of ZSH. By comparison, the pH in the bulk phase of ZS shows a gradual increase to 4.6, which is not alkaline enough for the formation of ZSH. The hysteresis of pH changes in bulk demonstrates that OH⁻ associated with interfacial hydrogen evolution will combine with Zn²⁺ at the interface to form ZSH rather than diffusing into the bulk phase due to the limited diffusion rate. This implies that it may be difficult to effectively suppress the interface parasitic side reactions for conventional pH buffer strategy only working in bulk electrolytes. Encouragingly, the rising rate and amplitude of pH are significantly reduced in both bulk phase and diffusion layer with the addition of NMI, suggesting the interfacial pH of electrolyte can be effectively stabilized by the interfacial pH-buffering strategy. In addition, the finite element method (FEM) is performed to simulate the pH distribution in diffusion layer during HER process. As shown in Figure 4f, constrained by the diffusion rate of OH⁻, the pH increases rapidly in the diffusion layer of ZS electrolyte, especially in the region near the interface, implying the rapid accumulation of ZSH on the surface. On the contrary, the pH remains uniform and stable (≈ 4.0) with the existence of NMIH⁺, demonstrating the interfacial pH-buffering strategy can significantly reduce the pH change of electrolyte, which is consistent with our above experimental results.

Hence, the pH-buffer process of additive can be summarized as follows: the specific adsorption of NMI and NMIH⁺ leads to the formation of a buffer layer on the interface, and the electrostatic effect will also drive the migration of NMIH⁺ toward the interface. Particularly, the NMIH⁺ ions absorbed on the interface will spontaneously release protons to obliterate ZSH and

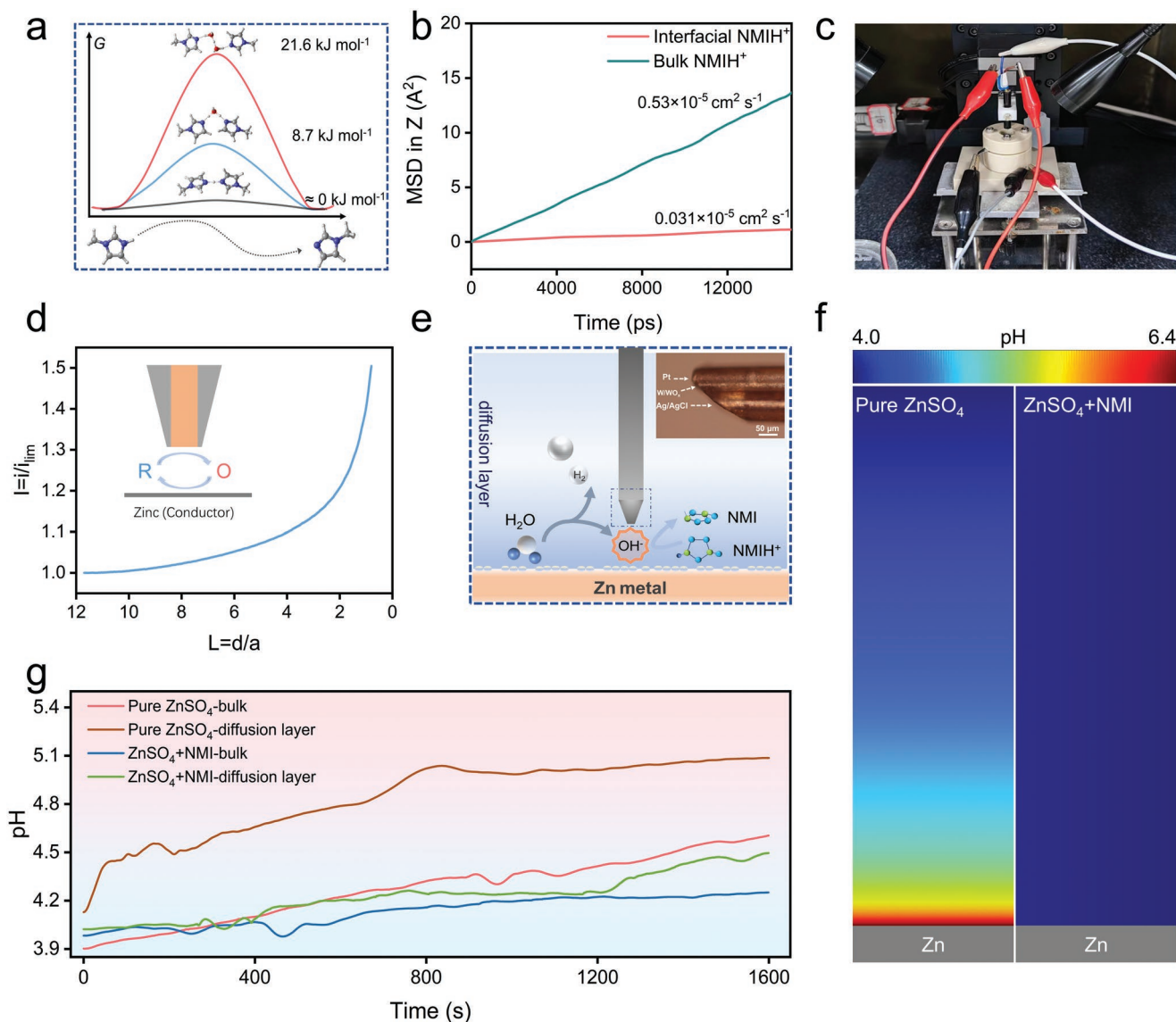


Figure 4. a) Activation Gibbs free energy of different proton-transport processes obtained by quantum chemistry calculation. b) Diffusion coefficients of NMIH⁺ in bulk and interface simulated by MD. c) Photo of in situ interfacial pH testing equipment. d) Approach curve of Pt probe above Zn substrate (inset is a diagram of positive feedback). e) Diagram of UME detecting pH changes (inset is a microscopy image of pH UME). f) pH distribution of diffusion layer in different electrolytes simulated by COMSOL. g) pH-time curves for bulk phase and diffusion layer of ZS and NZ tested by pH UME at a current density of 10 mA cm⁻².

convert themselves into NMI molecules when hydrogen evolution occurs. Subsequently, protons will be transported from the NMIH⁺ adjacent to interface to interfacial NMI through the direct proton-hopping process, thus maintaining the balance of NMI and NMIH⁺ at interface, and the equilibrium state in bulk will be achieved through diffusion and electromigration. Consequently, NMI molecules act as proton pumps to continuously transport protons from the bulk to the interface, thus maintaining a stable pH on interface and impeding the generation of ZSH.

Zn//–Zn symmetric cells are assembled to test the cycle stability of Zn anode with different electrolytes. As shown in **Figure 5a**, a symmetric cell cycled in NZ delivers a long lifespan of up to 2600 h at 1.0 mA cm⁻² with a plating–stripping capacity

of 1.0 mAh cm⁻², while the cell cycle in ZS happens a short circuit within 200 h due to the growth of dendrite. Moreover, the NMI additive can extend the lifespan of symmetric cell to 840 h under a harsh test condition (10 mA cm⁻², 10 mAh cm⁻²) (**Figure 5b**), corresponding to the extremely high cumulative plated capacity (CPC) of 4.2 Ah cm⁻², which is superior to the published works about electrolyte additives (**Figure 5c**, **Table S1**, **Supporting Information**). In addition, the symmetric cells employing NZ can achieve an ultralong lifespan of 1800 h at 2.0 mA cm⁻² for 2.0 mAh cm⁻² and 1000 h at 5.0 mA cm⁻² for 5.0 mAh cm⁻² (**Figure S18**, **Supporting Information**), demonstrating that the addition of NMI can realize the uniform deposition of Zn²⁺ in a wide range of current density. Moreover, when the thickness of Zn foils is reduced to 10 μm and 20 μm,

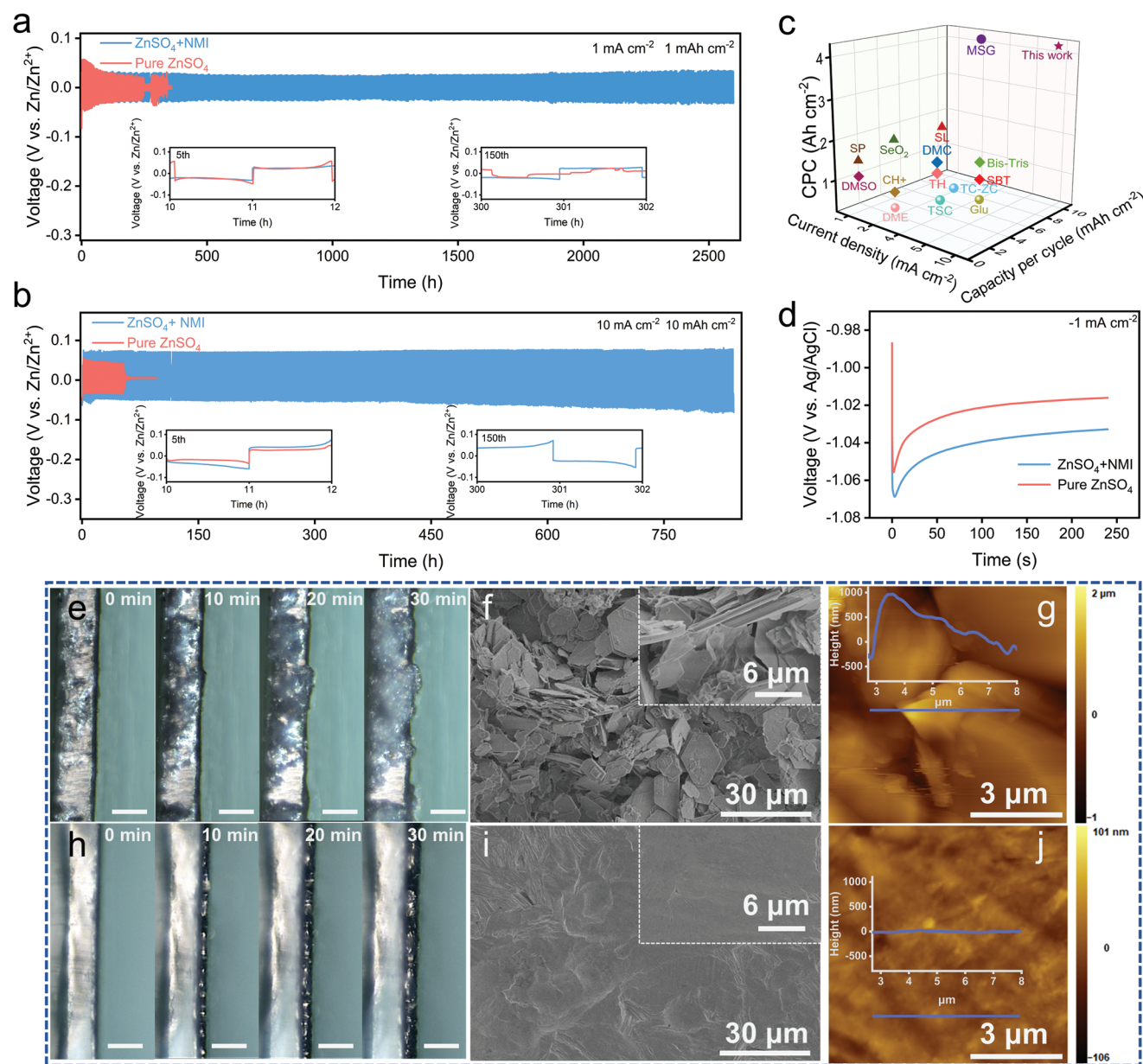


Figure 5. a,b) The voltage–time curves for Zn//–Zn symmetric cells with different electrolytes at 1.0 mA cm^{-2} with a plating–stripping capacity of 1.0 mAh cm^{-2} (a) and 10 mA cm^{-2} with a plating/stripping capacity of 10 mAh cm^{-2} (b). c) The CPC performance comparison of Zn//–Zn symmetric cells in NZ with previous additive works. d) Chronopotentiometry curve of Zn electrode in different electrolytes. e) In situ optical microscopy images of Zn deposition morphologies on the Zn electrode in ZS at a current density of 10 mA cm^{-2} . Scale bar: $100 \mu\text{m}$. f) Scanning electron microscopy (SEM) images and g) AFM images (inset is the corresponding height profiles for the blue segments) of Zn foil after 50 cycles in ZS at 1.0 mA cm^{-2} for 1.0 mAh cm^{-2} . h) In situ optical microscopy images of Zn deposition morphologies on the Zn electrode in NZ at a current density of 10 mA cm^{-2} . i) SEM images and j) AFM images of Zn foils after 50 cycles in NZ at 1.0 mA cm^{-2} for 1.0 mAh cm^{-2} .

symmetric cells with NZ electrolyte can also achieve outstanding performance (Figure S19, Supporting Information).

At the beginning of Zn electrodeposition, zinc clusters form on the surface of zinc anode first.^[33] It is demonstrated that the higher nucleation overpotential will bring the finer but larger number of nucleus on the surface, which will be beneficial for the uniform Zn electrodeposition.^[34] As shown in Figure 5d, both the nucleation overpotential and deposition overpotential on Zn electrode are increased by 20 mV with the existence of

NMI, revealing the adsorbed NMIH⁺ can reduce the nucleation radius due to the strong electrostatic interaction and steric hindrance. For subsequent stages of nucleus growth, Zn tends to be deposited on the original nucleus to minimize the surface energy.^[35] The increase of deposition overpotential with the addition of NMI (Figure 5d) suggests NMIH⁺ is adsorbed on the tip of nucleus due to the lowest potential, decreasing the local current density and inhibiting its further vertical growth.^[22b,36] Besides, the chronoamperometry (CA) curves

(Figure S20, Supporting Information) were tested with a negative overpotential (150 mV) on Zn electrode to evaluate the diffusion behavior of Zn^{2+} . The current density in ZS electrolyte changes continuously for 10 s after the mutation of potential, suggesting a random 2D diffusion process of Zn^{2+} .^[37] By contrast, the current density turns to stable rapidly with the addition of NMI, indicating the 2D diffusion is hindered by the dynamic absorption layer, thus inhibiting the inhomogeneity of ion field and dendrite growth.^[38] The in situ optical microscope is employed to monitor the Zn plating process in different electrolytes. As presented in Figure 5e and Video S1, Supporting Information, the initial Zn nucleation exhibits high randomness in ZS, leading to a loose and uneven electroplated layer. Whereas, beneficial from the higher nucleation overpotential and deposition overpotential, both the initial and subsequent deposition are significantly homogeneous and compact (Figure 5h, Video S2, Supporting Information), indicating the addition of NMI is beneficial for homogeneous deposition of Zn.

In fact, accumulation of insulated ZSH on the surface plays an neglected role in the failure of cells.^[39] Before the electrodeposition, lots of ZSH are accumulated on the Zn foils after immersion in ZS (Figure S21a, Supporting Information), which is harmful for the Zn electrodeposition.^[40] In contrast, NZ electrolytes can remove the passivation layer on the surface, and the NZ-soaked Zn foils can achieve small overpotential and better cyclic stability up to 700 h even with ZS electrolyte (Figure S21b, Supporting Information). In addition, the insulated ZSH accumulated on the surface during cycling will prevent the Zn plating and stripping, leading to a weak combination between the newly deposited Zn and the Zn substrate.^[41] Distinct Raman peaks at 1152, 1110, 1011, and 967 cm^{-1} are observed on the surface of Zn foils cycled in ZS electrolyte, which is corresponding to the existence of ZSH.^[42] (Figure S22a, Supporting Information) The Raman mapping is performed based on the peak intensity at 967 cm^{-1} . As presented in Figure S22b-e, Supporting Information, large amounts of ZSH distributes unevenly in the rough Zn cycled in ZS. And distinct S and O elements can be found on the surface of the Zn electrode by energy-dispersive spectrometry (EDS) analysis (Figure S23, Supporting Information). Due to the uneven initial deposition as well as the continuous accumulation of ZSH, lots of irregular flake deposits are observed on the surface of Zn electrode after 50 cycles in ZS (Figure 5f), and the atomic force microscopy (AFM) test (Figure 5g) reveals the surface altitude varies by several micrometers. As a result, the unconsolidated deposits will evolve into larger dendrites and pierce the separator in subsequent cycles, which is responsible for the short circuits of cells.^[43] Fortunately, as demonstrated in the Raman mapping and EDS tests, the introduction of NMI can significantly prevent the formation of ZSH. Consequently, the surface of Zn electrode is kept fresh during plating and stripping in NZ, thus ensuring a good combination between newly deposited Zn and the substrate. Finally, an ultradense morphology is formed on Zn electrode surface (Figure 5i), with a height variation of <200 nm (Figure 5j). Even after 100 cycles, the surface of Zn is still smooth with no dendrites appearing (Figure S24, Supporting Information). And the digital photos show that Zn foil after 50 cycles in NZ is silvery white with metallic luster

(Figure S25, Supporting Information), while the Zn foil cycled in ZS looks cinereous and rough.

Among the cathode materials of AZMBs, manganese oxides have been receiving extensive attention due to their environmental friendliness, abundant reserves, and high discharge voltage.^[44] To evaluate the availability of buffer strategy from NMI additive as well as the effect of anode improvement for practical application, polyaniline-intercalated manganese dioxide (MnO_2 -PANI, Figure S26, Supporting Information, reported by Xia's group^[45]) is employed as cathode material to fabricate full cells. It is worth noting that besides the Zn^{2+} insertion and proton insertion which are generally accepted as the discharge mechanisms of manganese oxide, recently many works have begun to focus on the conversion reaction between Mn^{2+} and MnO_2 .^[46] The two-electron redox reaction of $\text{MnO}_2/\text{Mn}^{2+}$ can provide an ultrahigh theoretical capacity of 616 mAh g^{-1} .^[47] Since the dissolution of MnO_2 is associated with the consumption of protons, ZSH will appear inevitably in weakly acidic ZnSO_4 aqueous electrolytes. However, the accumulation of ZSH is commonly regarded as the reason for capacity fading of both cathode and Zn anode, while strongly acidic electrolytes will aggravate the challenges of Zn anode.^[4b,47a] According to the specialty of NMI additive in reversibly releasing and capturing protons, it is predictably beneficial to accelerating the dissolution/deposition process.

All the full cells were tested with the addition of 0.2 M MnSO_4 in electrolyte. The linear sweep voltammetry (LSV) test (Figure S27, Supporting Information) indicates the window of 2.0 M ZnSO_4 + 0.2 M NMI + 0.2 M MnSO_4 (NZM) electrolyte is ≈ 2.3 V (vs Zn/Zn^{2+}), which is sufficient for full cells. As presented in Figure 6a,b, Figure S32b, Supporting Information, full cell employing NZM electrolyte exhibits an average discharge capacity of 234.7 mAh g^{-1} at 1.0 A g^{-1} in 200 cycles, which is nearly twice than the cell with 2.0 M ZnSO_4 + 0.2 M MnSO_4 (ZSM) electrolyte (119.9 mAh g^{-1}). Besides, the discharge capacities of full cells increase when more NMI is added (Figure S28, and Figure S32b, Supporting Information). Considering both the capacity and cyclic stability, 0.2 M NMI is also an appropriate concentration for the cathode. In addition, the average discharge capacity of a full cell with NZM electrolyte is 130.2 mAh g^{-1} at 2.0 A g^{-1} in 600 cycles (Figure S29, and Figure S32c, Supporting Information), while the cell with ZSM electrolyte has only an average discharge capacity of 91.5 mAh g^{-1} . At the current density of 0.5 A g^{-1} , full cell with NZM electrolyte exhibits an average discharge capacity of 288.5 mAh g^{-1} in 100 cycles, while that with ZSM electrolyte is 210.8 mAh g^{-1} (Figure S30 and Figure S32a, Supporting Information). Rate performance of full cells employing different electrolytes are presented in Figure 6c, Figure S31, and Figure S32d, Supporting Information. Full cell with NZM electrolyte exhibits an average discharge capacity of 365.7 mAh g^{-1} at 0.3 A g^{-1} , and it can still deliver an average discharge capacity of 112.2 mAh g^{-1} at a quite high current density (3.0 A g^{-1}). By contrast, the average discharge capacities of full cell with ZSM electrolyte are only 194.5 mAh g^{-1} and 83.7 mAh g^{-1} respectively under the same condition. Significantly, the discharge capacity of full cell with NZM electrolyte increases to 460.7 mAh g^{-1} when the current reduces to 0.3 A g^{-1} , which is higher than the theoretical capacity of one-electron redox reaction (308 mAh g^{-1}), verifying

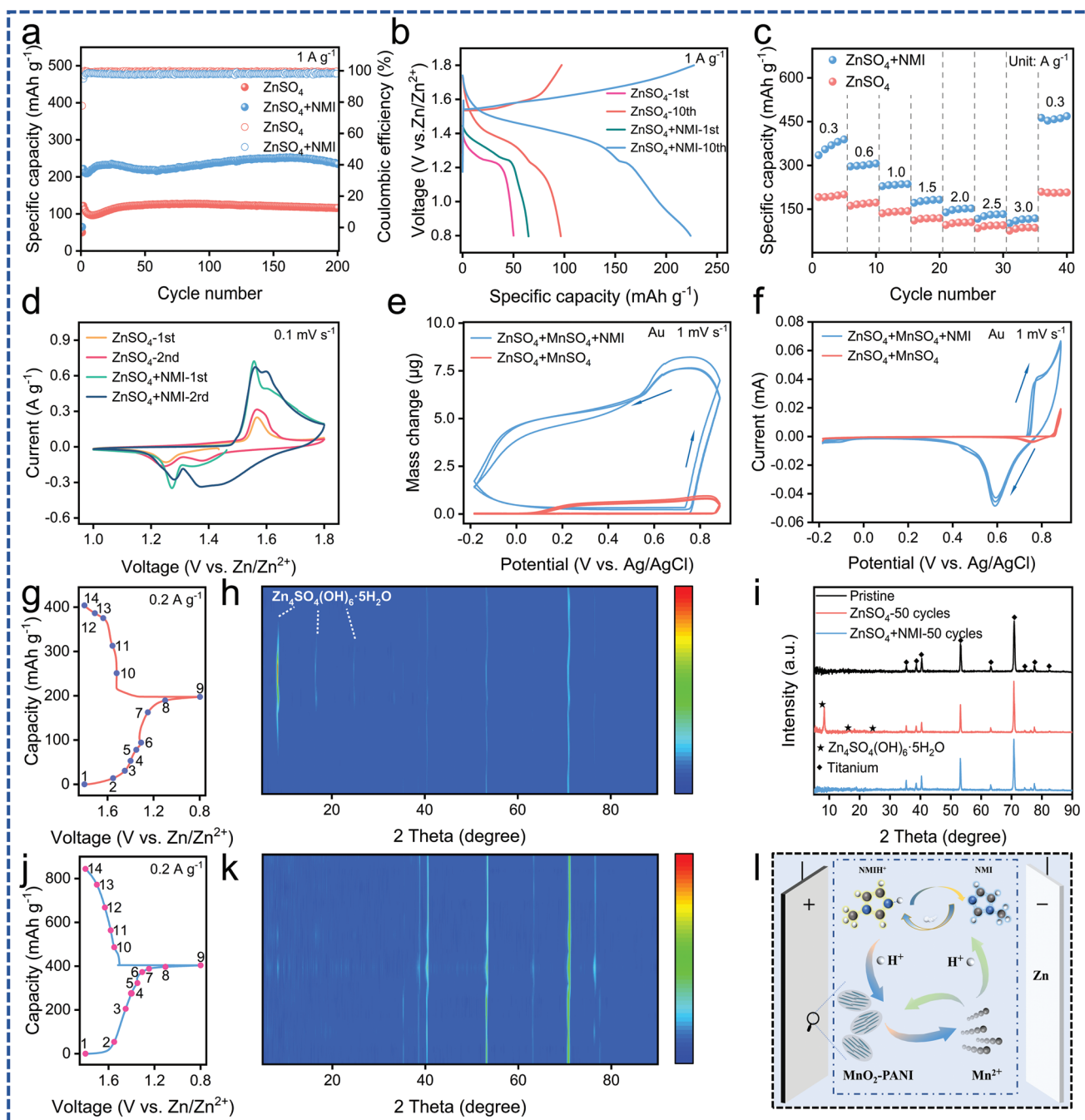


Figure 6. a) Cyclic performance of Zn//MnO₂-PANI full cells with different electrolytes at a current density of 1.0 A g⁻¹ and b) corresponding galvanostatic charge/discharge profiles. c) Rate performance of full cells with different tested current densities varying from 0.3 A g⁻¹ to 3.0 A g⁻¹. d) CV curves of MnO₂-PANI cathode in different electrolytes at 0.1 mV s⁻¹ and (f) corresponding CV curves. g,h,i,k) Ex situ XRD patterns of cathode during the second charge/discharge process in ZSM electrolyte (g,h) and NZM (j,k) electrolyte. i) XRD patterns of MnO₂-PANI cathode after 50 cycles at 1.0 A g⁻¹ in different electrolyte. l) The diagram of dissolution/deposition process between MnO₂ and Mn²⁺ with the addition of NMI.

there is a dissolution/deposition process between MnO₂ and Mn²⁺ in electrolyte.^[47b]

Furthermore, cyclic voltammetry tests for MnO₂-PANI cathode employing both electrolytes are performed to evaluate the role of NMI additive playing in the dissolution/deposition process. As shown in Figure 6d, the areas of both cathodic

peaks and anodic peaks performed in NZM electrolyte are nearly twice than the ZSM, indicating a significant improvement in discharge capacity. Interestingly, only one peak in CV test and one platform in the galvanostatic charge/discharge profile (Figure 6b) are observed in the first discharge process when tested in both electrolytes. Besides, the discharge capacity

of first cycle is much smaller than the subsequent cycle, verifying the discharge capacity in first cycle is mainly provided by the insertion of $\text{Zn}^{2+}/\text{H}^+$.^[46c] Since the conversion of $\text{MnO}_2/\text{Mn}^{2+}$ is ruled by the Nernst equation, potentials of dissolution or deposition process are determined by the concentration of protons.^[48] Besides, benefitting from the inhibited accumulation of ZSH on Zn anode toward the reduced Zn plating/stripping overpotential, the two cathodic peaks shift positively (1.24 V to 1.28 V and 1.37 V to 1.38 V) with the addition of NMI, and the anodic peak located at 1.57 V shifts negatively to 1.55 V, suggesting the full cell with NZM electrolyte has a higher discharge voltage and smaller polarization. As demonstrated in Figure S33a, Supporting Information, cathodic peak at 1.28 V disappears when ZnSO_4 is removed from the NZM electrolyte, indicating that there is only the dissolution/deposition process in $\text{MnSO}_4 + \text{NMI}$ electrolyte. Besides, areas of cathodic peaks and anodic peaks for $\text{MnSO}_4 + \text{NMI}$ electrolyte reach nearly half of that in NZM electrolyte, while the current in pure ZnSO_4 is quite weak, illustrating NMI can accelerate the dissolution/deposition process of $\text{MnO}_2/\text{Mn}^{2+}$ and thus providing half of extra capacity. Furthermore, the mass change of Au quartz electrode during charging and discharging process is tested in both electrolytes by EQCM within the potential window of $-0.184 - 0.886$ V (vs Ag/AgCl, 1.0–1.8 V corresponding to Zn/ Zn^{2+}). As can be seen from Figure 6e, a rapid increase of mass is observed at 0.757 V (vs Ag/AgCl) and the maximum mass change reaches to $7.6 \mu\text{g}$ in NZM electrolyte. By comparison, the mass changes at 0.862 V and the maximum mass change is only $0.85 \mu\text{g}$ in ZSM electrolyte, suggesting NMI additive can improve the kinetics of dissolution/deposition process. Besides, the mass of electrode can return to the pristine state, demonstrating the NMI additive can also enhance the reversibility of the dissolution/deposition process. Specifically, by integrating the CV curve of NZM in Figure 6f, it can be obtained that the quantity of electric charge consumed is 0.00762 C when the mass of electrode reaches the maximum for the first time, corresponding to $0.342 \mu\text{g}$ MnO_2 or $0.935 \mu\text{g}$ ZnMn_2O_4 . However, the actual test result is $0.76 \mu\text{g}$, indicating the formation of ZnMn_2O_4 intermedium during the dissolution/deposition process, which is consistent with the previous reports.^[46a,b]

In weakly acidic ZSM electrolytes, the proton-transport process is associated with the deposition and dissolution of ZSH.^[45] As shown in the ex situ XRD patterns of cathode during the second charge/discharge process in ZSM electrolyte (Figure 6g,h; Figure S34b, Supporting Information), very strong peaks indexed to ZSH appear at 8.1° , 16.2° , and 24.4° 2θ in the late stage of discharge and the early stage of charge, proving the formation of ZSH which is accompanied with the consumption of protons. However, the accumulation of ZSH on the surface of cathode is harmful to the kinetics of charge and discharge process. In contrast, with the existence of NMI additive, no obvious peaks indexed to ZSH appear in the XRD patterns (Figure 6j,k; Figure S34a, Supporting Information), declaring that NMIH^+ can neutralize the OH^- during the discharging process and thus avoiding the formation of ZSH. Even though the ZSH will dissolve during the charging process, XRD pattern in Figure 6i shows the obvious existence of ZSH on the surface of cathode after 50 cycles in ZSM electrolyte. By contrast, no ZSH peaks appearing suggests that the accumulation

of ZSH is distinctly inhibited by NMI additive, which is beneficial for the reversibility of discharging and charging process. According to above results, the evolution of NMI additive during the dissolution/deposition process can be described as follows (Figure 6l): During the discharge process, NMIH^+ will move toward the cathode interface and provide protons for the dissolution of MnO_2 , thus inhibiting the formation of ZSH and reducing the overpotential of full cells; During the charging process, the later-generated NMI will recycle the protons, hence decreasing the charging voltage and accelerating the oxidation of Mn^{2+} . The NMI additive participates in the proton cycle instead of solid by-product ZSH, thus significantly improving the kinetics and reversibility of dissolution/deposition process between MnO_2 and Mn^{2+} . As a result, NMI additive simultaneously realizes the improvement of the reversible Zn anode and MnO_2 -PANI cathode, and finally, a stable full battery with high specific capacity is obtained.

3. Conclusions

The enduring dynamically interfacial pH-buffering effect, which is realized through introducing NMI multifunctional additive as spontaneous proton pumps, is demonstrated by the characterizations of in situ pH UME technology, MD, and FEM simulations successfully. The buffer absorption layer constructed by NMI and NMIH^+ can not only prevent the accumulation of ZSH but also inhibit the growth of dendrite, thus improving the reversibility of Zn anode. Therefore, with the addition of 0.2 m NMI, the lifespan of Zn// $-\text{Zn}$ symmetric cells reaches up to 2600 h and Zn// $-\text{Cu}$ half cells deliver an ultrahigh average CE of 99.51%. In addition, due to the rapid kinetic of $\text{MnO}_2/\text{Mn}^{2+}$ deposition and dissolution process, Zn// MnO_2 -PANI full cell delivers an ultrahigh specific capacity of 234.7 mAh g^{-1} at 1.0 A g^{-1} . From a perspective of eliminating notorious by-products, strategy of interfacial pH-buffering solves one of the most stubborn aspects of zinc anode deterioration, which provides a new option for highly reversible Zn anode in practical application of AZMBs.

Supporting Information

Supporting Information is available from the Wiley Online Library or from the author.

Acknowledgements

The authors gratefully acknowledge the financial support from National Natural Science Foundation of China (No. 22109030 and 22021001), Fundamental Research Funds for the Central Universities (20720220073), The Key Research and Development Program of Yunnan Province (202103AA080019), Fujian Industrial Technology Development and Application Plan (202210002) and Guangdong Basic and Applied Basic Research Foundation (No. 2019A1515111069, No. 2021A1515010177). The authors acknowledge Ms. L.W. Lin in Xiamen Legang Materials Technology Co. Ltd for the pH UME and Tan Kah Kee Innovation Laboratory for the help of scientific tests. The authors would also acknowledge Beijing PARATERA Tech Co. Ltd. for providing HPC resources that have contributed to the research results reported within

this paper. URL: <https://paratera.com/>. The authors also acknowledge the help of Yu Qiao's group from Xiamen University on the DEMS tests.

Conflict of Interest

The authors declare no conflict of interest.

Data Availability Statement

The data that support the findings of this study are available from the corresponding author upon reasonable request.

Keywords

dissolution/deposition processes of MnO₂, EQCM and pH ultra-microelectrodes, interfacial pH-buffering strategy, N-methylimidazole, proton pumps

Received: September 20, 2022

Revised: December 4, 2022

Published online: March 4, 2023

- [1] a) M. Li, J. Lu, Z. Chen, K. Amine, *Adv. Mater.* **2018**, *30*, 1800561; b) G. L. Soloveichik, *Annu. Rev. Chem. Biomol. Eng.* **2011**, *2*, 503; c) P. Dai, X. Kong, H. Yang, J. Li, J. Zeng, J. Zhao, *ACS Sustainable Chem. Eng.* **2022**, *10*, 4381; d) J. Wang, S. Guo, X. Wang, L. Gu, D. Su, *J. Electrochem.* **2022**, *28*, 2108431.
- [2] a) Y. Tian, G. Zeng, A. Rutt, T. Shi, H. Kim, J. Wang, J. Koettgen, Y. Sun, B. Ouyang, T. Chen, Z. Lun, Z. Rong, K. Persson, G. Ceder, *Chem. Rev.* **2021**, *121*, 1623; b) N. Dong, F. Zhang, H. Pan, *Chem. Sci.* **2022**, *13*, 8243; c) R. F. Service, *Science* **2021**, *372*, 890.
- [3] a) H. Liu, J.-G. Wang, Z. You, C. Wei, F. Kang, B. Wei, *Mater. Today* **2021**, *42*, 73; b) J. Hao, X. Li, X. Zeng, D. Li, J. Mao, Z. Guo, *Energy Environ. Sci.* **2020**, *13*, 3917; c) Y. Liang, H. Dong, D. Aurbach, Y. Yao, *Nat. Energy* **2020**, *5*, 646; d) D. Kundu, B. D. Adams, V. Duffort, S. H. Vajargah, L. F. Nazar, *Nat. Energy* **2016**, *1*, 16119.
- [4] a) M. Li, Z. Li, X. Wang, J. Meng, X. Liu, B. Wu, C. Han, L. Mai, *Energy Environ. Sci.* **2021**, *14*, 3796; b) X. Jia, C. Liu, Z. G. Neale, J. Yang, G. Cao, *Chem. Rev.* **2020**, *120*, 7795.
- [5] a) W. Du, E. H. Ang, Y. Yang, Y. Zhang, M. Ye, C. C. Li, *Energy Environ. Sci.* **2020**, *13*, 3330; b) Q. Yang, Q. Li, Z. Liu, D. Wang, Y. Guo, X. Li, Y. Tang, H. Li, B. Dong, C. Zhi, *Adv. Mater.* **2020**, *32*, 2001854.
- [6] a) S. B. Wang, Q. Ran, R. Q. Yao, H. Shi, Z. Wen, M. Zhao, X. Y. Lang, Q. Jiang, *Nat. Commun.* **2020**, *11*, 1634; b) J. X. Zheng, Q. Zhao, T. Tang, J. F. Yin, C. D. Quilty, G. D. Renderos, X. T. Liu, Y. Deng, L. Wang, D. C. Bock, C. Jaye, D. H. Zhang, E. S. Takeuchi, K. J. Takeuchi, A. C. Marschilok, L. A. Archer, *Science* **2019**, *366*, 645.
- [7] a) Y. Yang, C. Liu, Z. Lv, H. Yang, Y. Zhang, M. Ye, L. Chen, J. Zhao, C. C. Li, *Adv. Mater.* **2021**, *33*, 2007388; b) Y. Yang, C. Liu, Z. Lv, H. Yang, X. Cheng, S. Zhang, M. Ye, Y. Zhang, L. Chen, J. Zhao, C. C. Li, *Energy Stor. Mater.* **2021**, *41*, 230.
- [8] a) P. Lin, J. Cong, J. Li, M. Zhang, P. Lai, J. Zeng, Y. Yang, J. Zhao, *Energy Stor. Mater.* **2022**, *49*, 172; b) J. Cong, X. Shen, Z. Wen, X. Wang, L. Peng, J. Zeng, J. Zhao, *Energy Stor. Mater.* **2021**, *35*, 586.
- [9] Y. Geng, L. Pan, Z. Peng, Z. Sun, H. Lin, C. Mao, L. Wang, L. Dai, H. Liu, K. Pan, X. Wu, Q. Zhang, Z. He, *Energy Stor. Mater.* **2022**, *51*, 733.
- [10] J. Cui, X. Liu, Y. Xie, K. Wu, Y. Wang, Y. Liu, J. Zhang, J. Yi, Y. Xia, *Mater. Today Energy* **2020**, *18*, 100563.
- [11] P. Sun, L. Ma, W. Zhou, M. Qiu, Z. Wang, D. Chao, W. Mai, *Angew. Chem., Int. Ed.* **2021**, *60*, 18247.
- [12] W. Xu, K. Zhao, W. Huo, Y. Wang, G. Yao, X. Gu, H. Cheng, L. Mai, C. Hu, X. Wang, *Nano Energy* **2019**, *62*, 275.
- [13] S. Guo, L. Qin, T. Zhang, M. Zhou, J. Zhou, G. Fang, S. Liang, *Energy Stor. Mater.* **2021**, *34*, 545.
- [14] J. Shin, J. Lee, Y. Park, J. W. Choi, *Chem. Sci.* **2020**, *11*, 2028.
- [15] a) Q. Yang, L. Li, T. Hussain, D. Wang, L. Hui, Y. Guo, G. Liang, X. Li, Z. Chen, Z. Huang, Y. Li, Y. Xue, Z. Zuo, J. Qiu, Y. Li, C. Zhi, *Angew. Chem.* **2021**, *133*, 940. b) D. Han, Z. Wang, H. Lu, H. Li, C. Cui, Z. Zhang, R. Sun, C. Geng, Q. Liang, X. Guo, Y. Mo, X. Zhi, F. Kang, Z. Weng, Q. H. Yang, *Adv. Energy Mater.* **2022**, *12*, 2102982.
- [16] N. Zhang, X. Chen, M. Yu, Z. Niu, F. Cheng, J. Chen, *Chem. Soc. Rev.* **2020**, *49*, 4203.
- [17] D. A. Carter, J. E. Pemberton, *J. Raman Spectrosc.* **1997**, *28*, 939.
- [18] B. Acharya, M. A. Sidheswaran, R. Yungk, J. Krim, *Rev. Sci. Instrum.* **2017**, *88*, 025112.
- [19] Y. Hussain, J. Krim, C. Grant, *Colloids Surf., A* **2005**, *262*, 81.
- [20] P. Kern, D. Landolt, *Electrochim. Acta* **2001**, *47*, 589.
- [21] a) Y. Su, J. Yan, M. Li, M. Zhang, B. Mao, *J. Phys. Chem. C* **2013**, *117*, 205; b) I. V. Voroshlyova, H. Ers, V. Koverga, B. Docampo-Álvarez, P. Pikma, V. B. Ivaništšev, M. N. D. S. Cordeiro, *Electrochim. Acta* **2021**, *379*, 138148.
- [22] a) R. Attias, B. Dlugatch, M. S. Chae, Y. Goffer, D. Aurbach, *Electrochem. Commun.* **2021**, *124*, 106952; b) Z. Hu, F. Zhang, Y. Zhao, H. Wang, Y. Huang, F. Wu, R. Chen, L. Li, *Adv. Mater.* **2022**, *34*, 2203104.
- [23] C. Zhen, S. Sun, C. Fan, S. Chen, B. Mao, Y. Fan, *Electrochim. Acta* **2004**, *49*, 1249.
- [24] Z. Long, A. O. Atsango, J. A. Napoli, T. E. Markland, M. E. Tuckerman, *J. Phys. Chem. Lett.* **2020**, *11*, 6156.
- [25] a) D. Marx, *ChemPhysChem* **2006**, *7*, 1848; b) M. Tuckerman, K. Laasonen, M. Sprik, M. Parrinello, *J. Phys. Chem.* **1995**, *99*, 5749.
- [26] a) L. Santos, J. P. Neto, A. Crespo, D. Nunes, N. Costa, I. M. Fonseca, P. Barquinha, L. Pereira, J. Silva, R. Martins, E. Fortunato, *ACS Appl. Mater. Interfaces* **2014**, *6*, 12226; b) S. J. Choi, S. Savagatrup, Y. Kim, J. H. Lang, T. M. Swager, *ACS Sens.* **2019**, *4*, 2593.
- [27] Z. Zhu, Z. Ye, Q. Zhang, J. Zhang, F. Cao, *Electrochem. Commun.* **2018**, *88*, 47.
- [28] a) Z. Guo, X. Jiang, X. Lin, *Anal. Sci.* **2005**, *21*, 101; b) K. Doi, N. Asano, S. Kawano, *Sci. Rep.* **2020**, *10*, 4110.
- [29] J. Kwak, A. J. Bard, *Anal. Chem.* **1989**, *61*, 1221.
- [30] C. G. Zoski, J. C. Aguilar, A. J. Bard, *Anal. Chem.* **2003**, *75*, 2959.
- [31] a) A. J. Bard, M. V. Mirkin, P. R. Unwin, D. O. Wipf, *J. Phys. Chem.* **1992**, *96*, 1861; b) P. Sun, M. V. Mirkin, *Anal. Chem.* **2006**, *78*, 6526.
- [32] V. V. Nikonenko, V. I. Vasil'eva, E. M. Akberova, A. M. Uzdenova, M. K. Urtenov, A. V. Kovalenko, N. P. Pismenskaya, S. A. Mareev, G. Pourcelly, *Adv. Colloid Interface Sci.* **2016**, *235*, 233.
- [33] V. Verma, S. Kumar, W. Manalastas, M. Srinivasan, *ACS Energy Lett.* **2021**, *6*, 1773.
- [34] a) H. Liu, Y. Zhang, C. Wang, J. N. Glazer, Z. Shan, N. Liu, *ACS Appl. Mater. Interfaces* **2021**, *13*, 32930; b) A. Pei, G. Zheng, F. Shi, Y. Li, Y. Cui, *Nano Lett.* **2017**, *17*, 1132; c) F. Yang, J. A. Yuwono, J. Hao, J. Long, L. Yuan, Y. Wang, S. Liu, Y. Fan, S. Zhao, K. Davey, Z. Guo, *Adv. Mater.* **2022**, *34*, 2206754.
- [35] T. Zhang, Y. Tang, S. Guo, X. Cao, A. Pan, G. Fang, J. Zhou, S. Liang, *Energy Environ. Sci.* **2020**, *13*, 4625.
- [36] X. Zeng, J. Liu, J. Mao, J. Hao, Z. Wang, S. Zhou, C. D. Ling, Z. Guo, *Adv. Energy Mater.* **2020**, *10*, 1904163.
- [37] M. Zhou, S. Guo, J. Li, X. Luo, Z. Liu, T. Zhang, X. Cao, M. Long, B. Lu, A. Pan, G. Fang, J. Zhou, S. Liang, *Adv. Mater.* **2021**, *33*, 2100187.
- [38] Z. Yang, C. Lv, W. Li, T. Wu, Q. Zhang, Y. Tang, M. Shao, H. Wang, *Small* **2022**, *18*, 2104148.

- [39] P. Xiao, H. Li, J. Fu, C. Zeng, Y. Zhao, T. Zhai, H. Li, *Energy Environ. Sci.* **2022**, *15*, 1638.
- [40] J. Hao, X. Li, S. Zhang, F. Yang, X. Zeng, S. Zhang, G. Bo, C. Wang, Z. Guo, *Adv. Funct. Mater.* **2020**, *30*, 2001263.
- [41] X. Zeng, J. Mao, J. Hao, J. Liu, S. Liu, Z. Wang, Y. Wang, S. Zhang, T. Zheng, J. Liu, P. Rao, Z. Guo, *Adv. Mater.* **2021**, *33*, 2007416.
- [42] Z. Zhao, R. Wang, C. Peng, W. Chen, T. Wu, B. Hu, W. Weng, Y. Yao, J. Zeng, Z. Chen, P. Liu, Y. Liu, G. Li, J. Guo, H. Lu, Z. Guo, *Nat. Commun.* **2021**, *12*, 6606.
- [43] J. Hao, J. Long, B. Li, X. Li, S. Zhang, F. Yang, X. Zeng, Z. Yang, W. K. Pang, Z. Guo, *Adv. Funct. Mater.* **2019**, *29*, 1903605.
- [44] H. Pan, Y. Shao, P. Yan, Y. Cheng, K. S. Han, Z. Nie, C. Wang, J. Yang, X. Li, P. Bhattacharya, K. T. Mueller, J. Liu, *Nat. Energy* **2016**, *1*, 16039.
- [45] J. Huang, Z. Wang, M. Hou, X. Dong, Y. Liu, Y. Wang, Y. Xia, *Nat. Commun.* **2018**, *9*, 2906.
- [46] a) H. Yang, D. Chen, J. Liu, Z. Yuan, M. Lu, W. Zhou, L. Shen, V. Shulga, W. Han, D. Chao, *Energy Environ. Sci.* **2022**, *15*, 1106; b) H. Chen, C. Dai, F. Xiao, Q. Yang, S. Cai, M. Xu, H. J. Fan, S. J. Bao, *Adv. Mater.* **2022**, *34*, 2109092; c) Z. Zhong, J. Li, L. Li, X. Xi, Z. Luo, G. Fang, S. Liang, X. Wang, *Energy Stor. Mater.* **2022**, *46*, 165.
- [47] a) C. Zhong, B. Liu, J. Ding, X. Liu, Y. Zhong, Y. Li, C. Sun, X. Han, Y. Deng, N. Zhao, W. Hu, *Nat. Energy* **2020**, *5*, 440; b) D. Chao, W. Zhou, C. Ye, Q. Zhang, Y. Chen, L. Gu, K. Davey, S. Z. Qiao, *Angew. Chem., Int. Ed.* **2019**, *58*, 7823.
- [48] Y. Liu, Z. Qin, X. Yang, J. Liu, X.-X. Liu, X. Sun, *ACS Energy Lett.* **2022**, *7*, 1814.